Laser-assisted water condensation in the atmosphere: a step towards modulating precipitation?

2012 J. Phys. D: Appl. Phys. 45 293001

(http://iopscience.iop.org/0022-3727/45/29/293001)

IOP PUBLISHING JOURNAL OF PHYSICS D: APPLIED PHYSICS

J. Phys. D: Appl. Phys. **45** (2012) 293001 (13pp) doi:10.1088/0022-3727/45/29/293001

TOPICAL REVIEW

Laser-assisted water condensation in the atmosphere: a step towards modulating precipitation?

J Kasparian[1], P Rohwetter[2], L Wöste[2] and J-P Wolf[1]

[1] GAP-Biophotonics, Université de Genève, Chemin de Pinchat 22, CH-1211 Genève 4, Switzerland
[2] Institut für Experimentalphysik, Freie Universität Berlin, Arnimallee 14, D-14195 Berlin, Germany

E-mail: jerome.kasparian@unige.ch

Received 22 February 2012, in final form 29 May 2012
Published 4 July 2012
Online at stacks.iop.org/JPhysD/45/293001

Abstract
We review the recent results about laser-induced condensation based on self-guided filaments generated by ultrashort laser pulses. After recalling the physico-chemistry of cloud particle formation in the atmosphere and the physics of laser filamentation, we discuss experimental results on laser-induced condensation and its relevance for modulating precipitation.

(Some figures may appear in colour only in the online journal)

1. Introduction

As a vital natural resource for life, water has been the object of attempts to control or modulate its cycle since ancient times. Such efforts primarily aimed at favouring its use via irrigation, seawater desalination or harvesting it from the atmosphere. They also focused on the prevention of disasters, such as flooding or damage caused by hail, and the prediction of atmospheric conditions.

Most civilizations developed magic or religious practice aiming at controlling the weather, and in particular precipitation. The first scientific attempts rely on the observation that clouds convert only a few per cent to a few tens of per cent of the available humidity into precipitation, leaving a wide room for improving the process 'yield'. The experiments date back to 1934, when the former Soviet Union launched programmes of airborne cloud seeding using calcium chloride [1]. After World War II, this activity developed further, with seeding by dry ice and silver iodide, both in the USSR and in the US with the well-known experiments from Langmuir and Schafer [2–4].

Since then, several approaches have been proposed in order to enhance precipitation by cloud seeding. Among them, *static* cloud seeding is both the oldest one [1–4] and still the most widespread today. It consists in injecting dry ice or silver iodide particles into cold clouds. Their molecular structure being close to that of ice helps in converting supercooled water droplets into ice, a state in which they are expected to grow faster. Alternatively, *dynamic* seeding aims at quickly converting supercooled water into ice particles in order to release latent heat that will in turn enhance convection and updrafts and finally allow the clouds to grow larger and harvest more water vapour from the atmosphere [5]. Finally, *hygroscopic* seeding of warm (e.g. tropical) clouds relies on the injection of artificial cloud condensation nuclei (CCN), i.e. droplet embryos of sub-μm to a few μm size, made of water or hygroscopic salts to produce water droplets. For example, large-scale experiments are conducted in that direction in Colorado [6]. The main challenge faced by this technique resides in adequately choosing the right embryo size and dispersing them efficiently while keeping them inside the active cloud volume. The latter difficulty can be addressed at least in part by using airborne pyrotechnic flares, which also have the advantage of reducing the required amount of necessary salt mass [7].

However, the efficiency of cloud seeding is still controversial [7–9]. This controversy is fuelled by the intrinsic variability of the atmosphere in both time and space, raising the need for large samples in order to obtain statistically significant results. In particular, the atmospheric variability and its dynamics make it extremely difficult to identify which seeding technique can be efficient and under which conditions [7].

This question may soon get an even broader scope. Ultrashort laser pulses were observed to generate highly hygroscopic species [10], resulting in the nucleation of nanometric and micrometric particles [11, 12]. This raised the prospect for laser-induced cloud seeding. Here, we review the recent results in this fast emerging field and discuss the applicability of laser-induced condensation to cloud seeding. This review is organized as follows. In section 3, we review the experimental results about laser-induced condensation, the interpretation and modelling of which is detailed in section 4. Finally, section 5 discusses the applicability of laser-induced condensation to cloud seeding and remote sensing. However, before directly discussing laser-induced nucleation, we will provide in section 2 an overview of the required background knowledge about both the physics and chemistry of particle formation in the atmosphere, and about the nonlinear propagation of intense ultrashort lasers and the resulting filamentation.

2. Background

2.1. Physico-chemistry of cloud particle formation in the atmosphere

Understanding the mechanisms of laser-induced condensation requires previous knowledge about the physico-chemistry of particle nucleation and water condensation. This section summarizes the essential data on this issue. For further details about nucleation in the context of atmospheric physics, the reader is referred to reference books [13, 14].

2.1.1. Thermodynamics of particle nucleation. In the context of atmospheric science, nucleation refers to the formation of condensed material (ice, liquid or aqueous phase) from the gas phase. In the following, we shall focus the discussion on liquid particles, which are more relevant in the lower troposphere, down to −20 °C. Nucleation is discontinuous, since a phase boundary is created between the forming liquid particle and the surrounding gas. It is called *heterogeneous* when it initiates on inhomogeneities such as pre-existing nanoparticles named *condensation nuclei* (CN), which have the ability to grow by harvesting matter from the gas to the liquid phase. Heterogeneous nucleation is supported by the abundance of atmospheric aerosols, especially in the troposphere. Conversely, nucleation occurring without CN is termed *homogeneous*. Homogeneous nucleation is called *homomolecular* if a single species is involved and *heteromolecular* if several species condense together.

The foundations of the classical nucleation theory [13, 14] were set by J W Gibbs in the second half of the 19th century. Phase changes between the liquid and gas phases separated by an infinite plane interface are thermodynamically favourable if they reduce the Gibbs energy of the whole system (i.e. both the gas and condensed phases) [15]: $G = U + pV - Ts$, where U is the internal energy, T and s are the temperature and entropy of the system, V is the volume it occupies and p is its pressure. By definition of the chemical potential μ, at a constant temperature and pressure, the Gibbs energy can also be derived from the chemical potential μ_i of each species i and the corresponding number of moles n_i:

$$G = \sum_{i=1}^{k} \mu_i n_i. \tag{1}$$

The chemical potential of gaseous species is obtained by considering them as ideal gases:

$$\mu_i(T) = \mu_i(T, p_o) + RT \ln\left(\frac{p_i}{p_o}\right), \tag{2}$$

where p_o denotes the standard pressure. The liquid phase is treated as the corresponding bulk liquid, ignoring effects of molecular orientation or conformation in nanometric clusters [16].

In the case of particle nucleation and growth, the Gibbs energy is not only defined by the chemical potentials, but it is also affected by the curvature of the interface between the liquid and gas phases, i.e. the particle surface. This influence stems from the surface tension, which is curvature-dependent. Its most important contribution to the Gibbs energy is the work needed to form the phase boundary. Considering a spherical droplet with radius r, the capillarity approximation yields a surface energy

$$G_{\text{surface}} = 4\pi r^2 \sigma, \tag{3}$$

σ being the surface tension of the bulk (i.e. for a plane, infinite surface). This positive term tends to increase the Gibbs energy, and hence to reduce the particle stability and condensation and oppose the particle growth. The total change in Gibbs energy due to the condensation of n moles of gas into a spherical liquid droplet can be expressed as

$$\Delta G = n(\mu_l - \mu_v) + \Delta G_{\text{surface}}, \tag{4}$$

where the subscripts l and v stand for the liquid and vapour phases, respectively. For ideal gases, the first term can be expressed in terms of the vapour pressure p_g and the saturation vapour pressure over a flat phase boundary p_g^o:

$$\mu_l - \mu_v = -RT \ln\left(\frac{p_g}{p_g^o}\right) = -RT \ln(S), \tag{5}$$

where S is called the *saturation ratio*, or relative humidity (RH) when expressed in percentage. If $S > 1$, considering that chemical potentials are smaller in the liquid phase ($\mu_l < \mu_g$), this term may balance the surface energy term, thermodynamically allowing condensation, i.e. particle growth. In the case of homogeneous homomolecular nucleation, equation (4) can be rewritten as

$$\Delta G = -\frac{4\pi}{3}\frac{k_B T}{v_l} \ln(S) r^3 + 4\pi r^2 \sigma, \tag{6}$$

where k_B is Boltzmann's constant, and v_l is the volume occupied per molecule in the liquid phase. In a supersaturated atmosphere ($S > 1$), ΔG reaches a maximum ΔG^* (or Gibbs energy barrier) at a so-called critical radius

$$r_{\text{crit}} = 2\frac{\sigma v_l}{k_B T \ln(S)}, \tag{7}$$

$$\Delta G^* = \Delta G(r_{\text{crit}}) = \frac{4\pi}{3}\sigma r_{\text{crit}}^2 = \frac{16\pi}{3}\frac{\sigma^3 v_l^2}{(k_B T \ln(S))^2}. \tag{8}$$

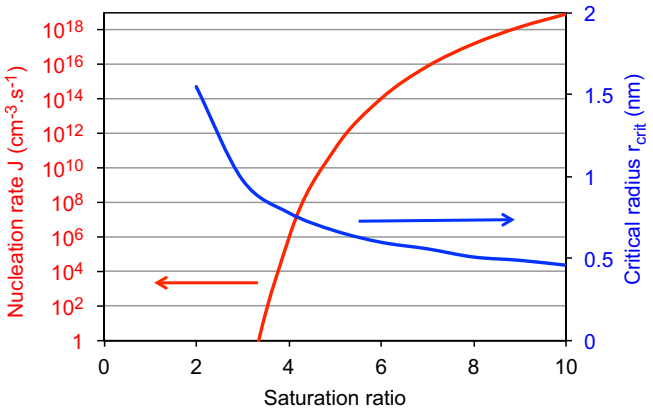

Figure 1. Homogeneous nucleation rate and critical radius for water at 20 °C, calculated using equation (11).

Since r_{crit} depends on the saturation ratio, one can alternatively define the equilibrium saturation ratio S_{eq} maximizing ΔG for a given radius r:

$$S_{\text{eq}}(r) = \exp\left(\frac{2\sigma v_l}{k_{\text{B}} T r}\right). \tag{9}$$

r_{crit} defines the criterion for particle stability at a given relative humidity, as an unstable equilibrium size between particle growth and evaporation. Particles below this radius will evaporate, while particles exceeding it tend to grow indefinitely until they deplete the water vapour available.

2.1.2. Homogeneous homomolecular nucleation. Homogeneous homomolecular nucleation relies on the collisions of water molecules due to thermal motion. Such collisions form dimers, which may subsequently collide with a third molecule to form a trimer and so on. Equation (6) allows the determination of the population of clusters as a function of the number of water molecules they contain, at thermodynamic equilibrium. The nucleation rate J can then be computed as the number of clusters per unit volume and time that exceed r_{crit}, thus entering in the growing regime:

$$J = A \exp\left[-\frac{\Delta G^*}{k_{\text{B}} T}\right], \tag{10}$$

where A depends on the partial vapour pressure of the condensing species and on the composition of the clusters. In the case of homomolecular homogeneous nucleation [14],

$$J = \left(\frac{2\sigma}{\pi m}\right)^{1/2} \frac{v_l N_{\text{g}}^2}{S} \exp\left[-\frac{\Delta G^*}{k_{\text{B}} T}\right]. \tag{11}$$

Here, N_{g} is the number density of vapour monomers and m the mass of a monomer. The term in $\ln(S)^{-2}$ in the definition of ΔG^* governs the strong dependence of J with saturation. As displayed in figure 1, homogeneous homomolecular nucleation is irrelevant for $S \leqslant 3$ under standard conditions, so that it plays no significant role under ambient conditions.

2.1.3. Homogeneous heteromolecular nucleation. While homomolecular homogeneous nucleation is inefficient under typical atmospheric conditions, the mutual dissolution of water with a hygroscopic species such as H_2SO_4 or HNO_3 substantially speeds up aggregation. The dissolution reaction reduces the Gibbs energy of the mixed liquid phase, reducing the equilibrium saturation ratio for each species. Considering two species a and b, the Gibbs energy change corresponding to the formation of a mixed nucleus can be expressed as

$$\Delta G(n_a, n_b) = n_a(\mu_{a,l}(n_a, n_b) - \mu_{a,v}) + n_b(\mu_{b,l}(n_a, n_b) - \mu_{b,v}) + \Delta G_{\text{surface}}(n_a, n_b), \tag{12}$$

$\Delta G(n_a, n_b)$ is saddle-shaped [17]. A binary droplet must grow across its ridge, which is most likely to occur close to the saddle point defining the effective Gibbs energy barrier of nucleation in the estimation of the nucleation rate (see equation (10)). The pre-exponential factor A depends on the actual path on the saddle surface and cannot be estimated *a priori*. Furthermore, the influence of mixing on the surface tension $\Delta G_{\text{surface}}$ [14] can be difficult to determine.

Heteromolecular homogeneous nucleation occurs efficiently and plays a key role in aerosol production and cloud formation in both the stratosphere and the troposphere. The H_2SO_4–H_2O system is the most important in that regard [18, 19, 29]. For example, stratospheric aerosols mainly consist of a concentrated aqueous solution of sulfuric acid, supercooled down to −85 °C. A major fraction of tropospheric particles below 1 μm are also sulfuric [20]. This importance is due to the fact that sulfate is both highly hygroscopic and relatively abundant (5–300 ppt in clean atmosphere, up to 10 ppb in polluted areas) [14]. SO_2 from biogenic (80%), volcanic and fuel burning origins [20] is oxidized into SO_3 by OH radicals, and then quickly reacts with H_2O, yielding H_2SO_4 [14].

Binary nucleation of as little as 4×10^7 cm^{-3} H_2SO_4 molecules and various organic compounds oxidized by OH radicals was also observed under natural conditions, under which tropospheric nucleation can be observed [21]. The chemical affinity of the two species is so high that the critical nuclei contained only one molecule of H_2SO_4 and one of the organic species, resulting in nucleation rates one to two orders of magnitude faster than the classical H_2SO_4–H_2O binary nucleation [22].

In additon to H_2SO_4, the main hygroscopic species contributing to water condensation in the atmosphere is HNO_3 resulting from the oxidation of NO and NO_2, the concentration of which varies from 0.02 to 1000 ppb in urban areas. As will be discussed later, this pathway can be strongly enhanced by laser irradiation.

2.1.4. Heterogeneous nucleation. Aerosol particles are abundant (up to several 10^3 cm^{-3}, or even more in urban areas) in the atmosphere, especially in the lower troposphere. These pre-existing solid particles offer a large active surface area per unit air volume, acting as favourable sites for impinging water molecules from the gas phase. Adhesion of these molecules on the particle substrate balances surface tension and reduces the Gibbs energy needed to transfer molecules from the gas phase to the liquid phase. Surface diffusion of condensing

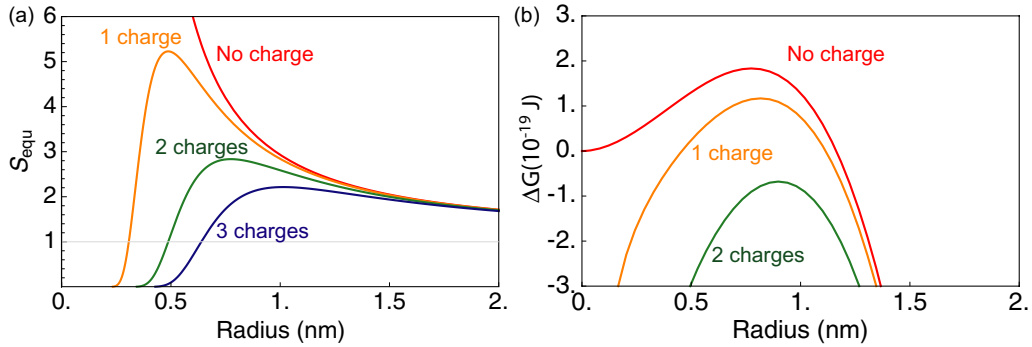

Figure 2. Effect of charge on particle stability at 20 °C. (*a*) Equilibrium saturation ratio of charged water particles; (*b*) Gibbs energy barrier of charge-stabilized water particles at 100% RH.

molecules may also help them to gather into a liquid nucleus on this surface. The Gibbs barrier is even further reduced by the solvation energy if the aerosol particles are soluble in water, resulting in an abrupt transition from solid to liquid when the RH rises above a so-called deliquescence relative humidity (DRH), which is as low as 75% for NaCl, 40% for NH_4HSO_4 and 0% for H_2SO_4 at 298 K [14]. In the latter case, 0% DRH means that water uptake can occur at any RH.

The efficiency of heterogeneous nucleation reduces the critical saturation ratio in the atmosphere to 102% or even below [23]. The presence of aerosol can therefore suppress homogeneous nucleation by harvesting both the needed water and the hygroscopic species from the gas phase.

2.1.5. Ion-induced nucleation. In the early 20th century, following the demonstration of the Wilson chamber [24], electric charges were found to reduce the threshold saturation ratio for droplet nucleation [25, 26] by lowering the Gibbs energy for a vapour molecule entering a charged cluster. Because of the large dielectric constant of water, it is treated as a conductor in the classical Kelvin–Thomson (CKT) equation describing charge-assisted nucleation. This equation defines the equilibrium vapour saturation ratio over a charged liquid surface, including the contribution of surface curvature discovered by Lord Kelvin. However, Tohmfor and Volmer found that experimental data are better reproduced if water is treated as a dielectric sphere [26]:

$$S_{\mathrm{CKT}} = \exp\left[\frac{m_{\mathrm{v}}}{k_{\mathrm{B}}T\rho_{\mathrm{H_2O}}}\left(\frac{2\sigma}{r} - \frac{(1-\varepsilon_{\mathrm{H_2O}}^{-1})q^2}{32\pi^2\varepsilon_0 r^4}\right)\right] \qquad (13)$$

considering a value of $\varepsilon_{\mathrm{H_2O}} \simeq 1.85 \ll \varepsilon_{\mathrm{H_2O,bulk}} \simeq 80$. This deviation from the bulk dielectric constant is due to the reorientation of the permanent dipole moments of the water molecules in the charged particles. However, as displayed in figure 2, a reasonable amount of charges per particle cannot stabilize clusters beyond a few molecules, except at very high supersaturation well beyond typical atmospheric conditions [27].

While direct charge-induced water nucleation is not relevant under normal atmospheric conditions where the saturation ratio cannot exceed 1.02 [28, 29], modern models of heteromolecular homogeneous nucleation now include effects of electrical charge [18, 19] and suggest that ions have an important role in the homogeneous binary H_2SO_4–H_2O nucleation even in the planetary boundary layer, where it competes with efficient heterogeneous nucleation [19].

2.1.6. Activation of atmospheric particles. Particles are said to be *activated* or qualified as *droplets* if they exceed the critical radius (see equation (7)), and can, in principle, grow indefinitely. Activation may result either from a rise in the RH, or from a change in the chemical composition of the surrounding atmosphere, influencing that of the particle, e.g. by allowing the uptake of hygroscopic species such as HNO_3 or H_2SO_4. Unactivated particles are referred to as *haze* in the context of cloud physics. Particles that can get activated at a RH below the threshold of homogeneous nucleation are named *condensation nuclei* (CN). Among them, those that get activated at atmospherically relevant RH (up to 102%) are named *cloud condensation nuclei* (CCN) [14].

Close to 100% RH, tropospheric air contains wet background aerosol, the larger of which can heterogeneously nucleate water vapour at RH slightly above 100% [13], qualifying them as CCN. Even in clean maritime air, their concentration is close to 100–1000 cm^{-3}. They have diameters in the range 50–140 nm, depending on their contents in soluble material.

2.2. Laser filamentation

Laser filamentation is a propagation regime typical of high-intensity, ultrashort laser pulses. Filamentation in air was discovered accidentally by Braun *et al* [30] in an attempt to use such pulses for remote sensing: unexpectedly, slightly focused 200 fs pulses of 'moderate' peak power (13.5 GW) collapsed and damaged remote optical components. They interpreted this phenomenon as a trapped state of self-focusing, balanced by the defocusing lens induced by the negative refractive index contribution of the free electrons from the low-density plasma generated in air at the self-focus.

This dynamical balance between non-linear contributions to the refractive index featuring different orders, hence different intensity dependences, is indeed the basis of today's understanding of laser filamentation [31–33]. It ensures stable, quasi-solitonic propagation of laser filaments over distances

Figure 3. Multiple filamentation of a 3 J, 30 fs laser pulse of 10 cm diameter, imaged in real colour on a screen.

up to hundreds of metres [34], with an intensity clamped close to 50 TW cm^{-2} [35, 36], allowing efficient ionization of the propagation medium, as well as the initiation of multiphoton-excited photochemistry. This clamping intensity is understood theoretically as ensuring the dynamic balance between focusing by the Kerr self-focusing on the one side, and plasma defocusing [37] as well as the higher order Kerr effect (HOKE) [38, 39] on the other.

The initiation of laser filamentation requires the Kerr self-focusing to balance diffraction, so as to initiate the beam collapse. This occurs as soon as the power exceeds a so-called *critical power*, which amounts to a few GW in air for 800 nm pulses [40]. Under typical conditions, because of losses, spatial and temporal inhomogeneities of the beam and other perturbations, up to 5 critical powers are required to initiate one filament. If the laser power is further increased beyond this value, the number of laser filaments increases almost linearly with the incident power, and multiple filaments are generated in the beam (figure 3) at a typical rate of 1 filament for each 5 critical powers [41]. However, this increase is limited by the cross section of the beam profile. Each filament typically needs about 1 mm^2 of beam cross-section to develop with its surrounding photon bath, so that the filament number density saturates [42], resulting in an increase in the photon bath intensity that may even end up in its efficient contribution to non-linear processes [43].

Laser filaments can be generated at kilometre-range distances [44, 45] by adequately tailoring the laser pulses. The main parameters at hand are the beam diameter and focusing, as well as the pulse chirp [46], i.e. the temporal offset of its spectral components related to one another. If the initial pulse chirp is opposite to the atmospheric group-velocity dispersion, the pulse will tend to re-compress at a distance that depends only on the magnitude of the chirp, and can therefore be easily set on demand. From the technical point of view, this is realized easily in chirped pulse amplification (CPA) lasers [47] by slightly varying the distance between the gratings of the compressor.

Furthermore, this long-distance capability can efficiently be exploited for atmospheric applications because of the unexpectedly high robustness of the dynamic balance at the root of filamentation. Filaments have the unique capability to self-heal after being blocked by an obstacle like a water drop because they are replenished by the surrounding photon bath (also known as energy reservoir [48]) [49–51]. Conversely, a diaphragm blocking this photon bath arrests filamentation [48]. They can therefore propagate efficiently not only through rain, or fog [41], but also through reduced pressures [52] and highly turbulent regions [53, 54] without being substantially perturbed. This robustness makes filaments highly suitable for applications in the atmosphere [55, 56], which is intrinsically a perturbed propagation medium.

Atmospheric applications have been investigated by several groups, with even real-scale outdoor experiments allowed by the mobile-terawatt laser *Teramobile* [46] or the T&T lab [57]. For example, the *Teramobile* produces 800 nm pulses of up to 350 mJ energy in pulses as short as 70 fs, at a repetition rate of 10 Hz. It has the unique property of being embedded in a standard 20 ft freight container equipped with a standard optics laboratory, including air conditioning, vibration control, as well as electrical power and cooling water management.

The first family of applications of filaments aims at using them to improve remote sensing or analysis. The most natural one in this regard is light detection and ranging (Lidar). In this technique (figure 4(*a*)), a laser pulse is emitted into the atmosphere, and the backward-scattered light is collected by a telescope and recorded as a function of the pulse time of flight, i.e. of distance. The detected light bears information about the transmission as well as the backscattering efficiency by the air molecules (Rayleigh scattering) and by the aerosol particles (Mie scattering). Lidar strongly benefits from the broad supercontinuum [58] generated by the filaments, which ranges from 230 nm in the ultrviolet [59] up to 14 μm in the mid-infrared [60]. This continuum covers absorption bands of most atmospheric pollutants, including ozone, NO_x, SO_2, benzene, toluene and other volatile organic compounds (VOCs), opening the way to their simultaneous sensing by a white-light Lidar [61]. The white-light continuum can be produced either directly in the laser filaments [62], or in a krypton gas cell prior to its emission into the atmosphere [63]. Multispectral Lidar (figure 4(*b*)) also provides multichannel information suitable for determining the size distribution of atmospheric aerosols, together with a simultaneous measurement of atmospheric temperature and humidity [64]. This technique, which leaves the atmosphere unaffected, provides a comprehensive meteorologically relevant characterization of the atmosphere. This approach using a single laser system potentially offers an unlimited number of information channels in contrast to conventional multispectral Lidars using several independent lasers, each one providing a single wavelength.

An even more powerful variant of femtosecond Lidar takes benefit of the high intensity conveyed by the filaments

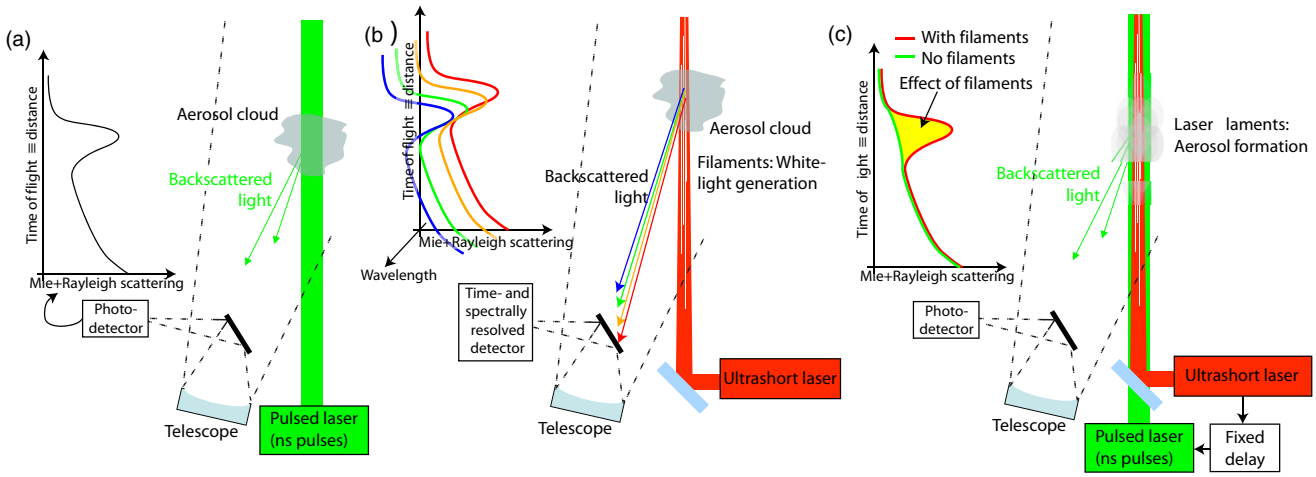

Figure 4. (*a*) Principle of Lidar. Laser pulses are emitted into the atmosphere. The backscattered light bears information about the size and number density of the encountered aerosol particles, via their Mie backscattering cross-section. (*b*) Principle of multispectral (or white-light) Lidar. Filaments generate a broad spectrum upstream of the region to be analysed, which is left unaffected by the laser but scatters back each wavelength to the detection device. (*c*) Principle of pump-probe Lidar. Particles are produced *in situ* by ultrashort laser filaments in the atmosphere, depending on the atmospheric conditions. These particles are probed after a predefined delay by a Lidar with a beam collinear with the filaments.

to non-linearly excite the species to be analysed. Two-photon fluorescence Lidar was applied to remotely detect and identify biological simulants in aerosol droplets [65]. This technique has several advantages over one-photon excited fluorescence-based Lidar, which requires an ultraviolet pump wavelength. The infrared pump is less attenuated by the atmosphere than the ultraviolet, which is much more Rayleigh-scattered (with λ^{-4} wavelength dependence) and absorbed by ozone, a drawback which is particularly acute in urban environments where aerosol monitoring is the most relevant. Furthermore, in spherical particles, the non-linear processes, such as multiphoton-excited fluorescence, are preferentially emitted backward due to the internal focusing effects in the particles [66]. This backward emission is particularly favourable for remote sensing since the signal is preferentially emitted towards the detection device.

Multiphoton-excited fluorescence was also proposed to remotely detect gaseous pollutants in the atmosphere [67]. Here, the main advantage resides in the so-called 'clean fluorescence' [68]: due to their low energy for a given peak power, the femtosecond pulses heat the medium very little, so that the fluorescence lines can be detected on a baseline almost free of thermal contributions. The same advantage, as well as the unique capability of the laser filaments to deliver a high intensity at remote distances regardless of diffraction, is at the root of remote filament-induced breakdown spectroscopy (R-FIBS), a variant of laser-induced breakdown spectroscopy (LIBS), in which the material to be analysed is illuminated by a focused laser beam and the spectrum of the plasma excited at the ablation point is spectrally recorded to provide elemental analysis. Using laser filaments, we detected LIBS signals from several metal samples at a distance of almost 200 m [69], with a very favourable distance scaling since the filaments provide an extended focus with an intensity clamped independently from the propagation distance. The possibility of performing remote measurements together with the fact that LIBS needs no sample preparation make R-FIBS very suitable for the monitoring and/or sorting of dangerous items such as nuclear waste, mapping minerals in hard-to-access locations in open-sky mines, or monitoring hot alloy production. This technique was also applied to analyse stone surfaces in cultural heritage buildings [70], as well as explosive simulants [71].

Beyond sensing the atmosphere, ultrashort laser pulses have the unique capability to influence it due to the generation of an underdense plasma channel with typically 10^{15}–10^{16} electrons cm^{-3} over up to hundreds of metres [34], with a typical diameter of 100 μm, offering a typical resistivity of $1\,\mathrm{M\Omega\,m^{-1}}$. This plasma channel strongly contrasts with the plasma sparks generated by longer pulses. In the latter, the typical nanosecond pulse duration allows efficient avalanche ionization, resulting in a dense plasma opaque to the laser and preventing the generation of any long conducting channel: even high-energy (several kJ) CO_2 lasers could guide lightning strikes only with great difficulty [72, 73]. In contrast, the plasma channels generated by ultrashort laser pulses trigger and guide megavolt-range discharges over several metres [74, 75], reducing the breakdown voltage by typically 30% and offering a straight discharge along the laser beam. Small-scale demonstrations were also performed with UV pulses [76]. Pulse sequences, which enhance the plasma lifetime, further improve the triggering efficiency [77, 78]. These results open the prospect not only for guiding lightning strikes [79, 80], but also to remotely measure the electric field [81]. Mapping this atmospheric parameter in three dimensions is critically important to understand and model the physics of lightning, but very difficult to measure with classical instruments, which tend to locally perturb the field under measurement.

However, the most spectacular application of femtosecond pulses in the atmosphere is probably laser-induced condensation.

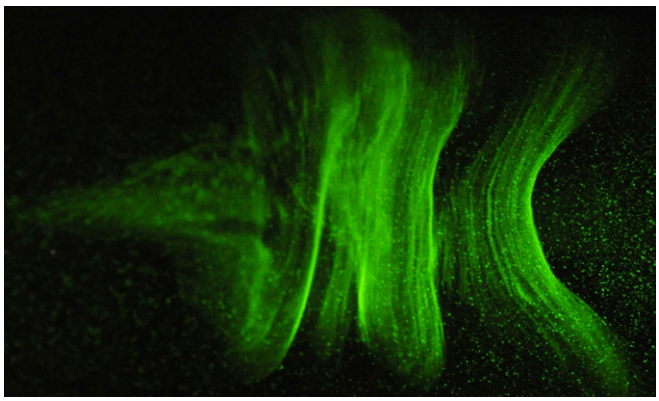

Figure 5. True-colour image of laser-induced condensation in a cloud chamber, illuminated by a green auxiliary laser. The main laser features 20 mJ pulses in 60 fs pulse duration, at a repetition rate of 100 Hz, and is shot continuously over a few minutes. The image is taken with 1600 ISO and an exposure time of 67 ms. The cloud has a transverse dimension in the centimetre range. Its deformation reveals the air turbulence induced by the blast due to the energy deposited by the laser filament in the atmosphere.

3. Observation of laser-induced condensation

3.1. Laboratory results

The possibility of inducing condensation in a supersaturated atmosphere with laser filaments was mentioned for the first time in 2003, as a way to detect supersaturation [55]. In a first qualitative experiment, the *Teramobile* team reported strong droplet formation in a cloud chamber saturated with water or isopropanol and illuminated by near-IR laser pulses (800 nm). The effect was so strong that it was clearly visible with the naked eye, also revealing the turbulent motion of the air blasted by the energy locally deposited by the filament (figure 5). Under similar conditions ($-29\,^{\circ}$C, RH $\sim$130%), laser filaments were observed to produce particles up to 300 μm, which subsequently sedimented and accumulated within 30 min as snowflakes on the cold baseplate of the cloud chamber under the laser beam [82]. Strong particle formation was also independently reported in 2005 with 10 ns pulses of up to 250 mJ in the ultraviolet at 193 nm [83].

These first observations were, however, not made quantitatively until 2010 [11]. Launching laser filaments in a cloud chamber at a temperature of $-24\,^{\circ}$C and 230% RH yielded reproducible and spectacular cloud trails along the laser beam. An optical particle sizer revealed three modes in the size distribution: 4, 50 and 250 μm diameter. These modes also evolved differently after the laser shots. The water contents of the smaller mode remained almost constant. The small particles coalesced, so that their population dropped by half, while the average diameter grew up to 6 μm. Simultaneously, the medium-sized mode efficiently gained water, with its particles growing from 50 μm to 80 μm in diameter within 3 s and doubling their number density. This increase was sustained by the laser-induced fragmentation of particles from the larger mode, the remaining particles of which grew up to 400 μm. As a result, the total condensed water content of the chamber atmosphere increased, in the active volume, by a factor of 100 within 3 s, denoting a condensing rate as high as 5 mg cm^{-3} s^{-1}.

More interestingly, laser filaments also had a dramatic effect under *sub-saturated* conditions. Illuminating the air inside the cloud chamber increased the optical scattering signal by a factor of 25, revealing substantial condensation of water particles within 4 s, i.e. only 40 laser shots.

3.2. Field measurements

The same effect was later observed directly in the atmosphere with a relative humidity of 90–93%, and an extremely low background aerosol level, as evidenced by the 70 km horizontal visibility [11]. The beam of the *Teramobile* laser was launched vertically. The aerosols were monitored by a classical Lidar synchronized with the femtosecond laser. Between 45 and 75 m height, where the filaments were strongest, their Mie backscattering increased by a factor of 20 when the filamenting beam was active, reaching a value typical of haze ($\beta_{\mathrm{Mie}} = 2 \times 10^{-5}$ m^{-1} sr^{-1}) [61].

Beyond this demonstration, we gathered a wealth of quantitative data about laser-induced condensation in the atmosphere under a wide range of temperatures (2–36 $^{\circ}$C) and RH (35–100%) [12] during a 6-month campaign in Geneva. We compared the particle density close to the laser beam with that at a reference location (figure 6). A laser-induced increase in the particle number density is observed over a wide range of diameters, up to a few tens of μm. The effect is most spectacular for particles of $\sim$25 nm diameter. At 75% RH, the laser multiplied their number density by a factor of 3–6, exceeding 10^5 cm^{-3} close to the filaments. Simultaneously, the concentration of 10 μm particles increased by 30%. The laser-generated particles were stable over more than 20 min.

The particle generation is accompanied by efficient ozone formation, denoting the activation of efficient plasma chemistry. This chemistry influences particle formation: ionic chromatography analysis of the laser-generated particles impacted on Teflon filters evidenced high concentrations of HNO_3, a hygroscopic molecule detected as dissolved NO_3^- ions in concentrations two orders of magnitude above that of SO_4^{2-} in the same particles [12].

This laser-induced particle formation depends strongly on the water volume mixing ratio (VMR) and RH of the atmosphere, but in a contrasted way for different particle sizes. Figure 7 displays the correlations between the fluctuations of the atmospheric temperature and RH on one side, with those of the number concentrations of laser-induced particles of each diameter class. The laser-induced formation of particles below 400 nm correlates with the relative humidity, which can be understood by recalling that the RH determines their thermodynamic stability. Conversely, a second regime emerges for particles above 2 μm, which are correlated with water VMR. The latter defines the number of water molecules available per unit volume in the atmosphere to feed the particle growth (see section 4.2).

3.3. Scaling of the condensation yield with laser parameters

The power dependence of the laser-induced particle generation is critical to go beyond small-scale demonstrations and to

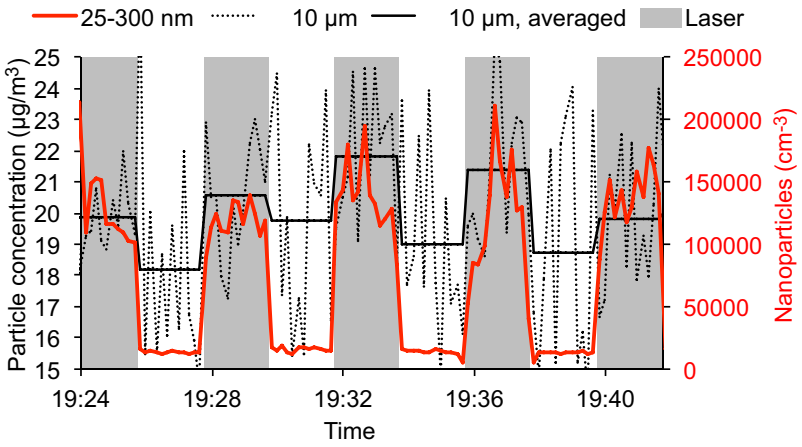

Figure 6. Quantitative observation of laser-induced condensation at 70% RH. The particle concentration is alternatively sampled close to the laser beam and under reference conditions. The difference between the measured concentrations is attributed to the effect of the laser.

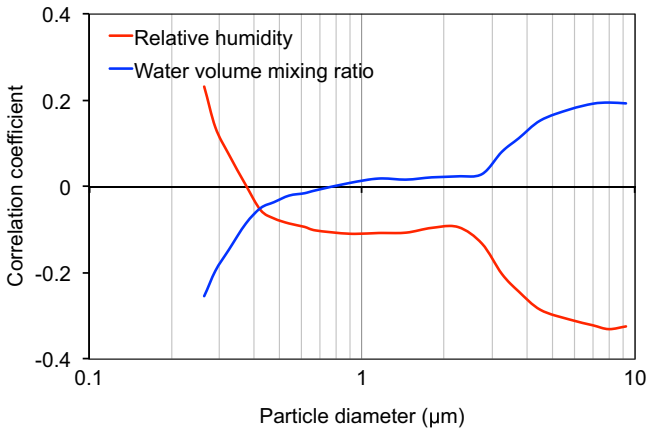

Figure 7. Dependence of the concentration of laser-induced particles of various sizes on the relative humidity and water mixing ratio (after [12]). The graph displays the correlation of the effect of the laser for each size with the considered atmospheric parameter.

dimension future systems for potential real-scale applications. Experiments in that regard have been performed on several laser systems, from tabletop systems to terawatt systems (*Teramobile* [46]), and even to the 100 TW-level (DRACO, 30 J, 100 TW) [84].

At 'low' intensity, slightly above the threshold for filamentation, the nanoparticle production is proportional to the incident intensity, i.e. to the filament number [37, 38, 85]. However, above ~500 GW cm^{-2}, the filament number saturates [42] but simultaneously, the number density of nanoparticles increases faster than linearly with the incident intensity. This fast rise is a consequence of an increasing contribution of the photon bath [84] with a fifth (multiphoton dissociation of oxygen leading to the formation of ozone) to eighth-order (ionization of O_2) non-linearity [86].

Furthermore, a third contribution, proportional to the fluence of the photon bath rather than to its intensity, was identified in the case of strongly chirped pulses (i.e. in the picosecond range) [84]. Finally, neither the sign of the chirp nor the incident polarization (linear or circular) influences the laser-induced condensation [87]. In contrast, a cumulative effect was suggested by the observation that particle production is more efficient when the laser is emitted as a regular pulse train as compared with the same number of pulses grouped in bursts [82].

4. Mechanism of laser-induced condensation under atmospheric conditions

4.1. Laser-induced production of hygroscopic trace gases

According to the Thomson mechanism [25, 26], at high supersaturation ratios, the 10^{15}–10^{16} cm^{-3} charges generated in the laser filaments efficiently trigger nucleation. But as detailed in section 2.1.4 this mechanism is irrelevant under atmospheric conditions, as confirmed experimentally by the different intensity dependences of nanoparticle production and the electron generation in the filaments [87]. Rather, the initiation of laser-induced condensation relies on photodissociative processes. For example, only 7 photons at 800 nm are required to photodissociate N_2, as compared with 11 photons to ionize it [88, 89]. Even fewer photons are required at shorter wavelengths, allowing UV light produced by either a nanosecond argon laser or a mercury lamp to efficiently induce condensation [90].

These photochemical processes allow laser filaments to produce considerable amounts of O_3 and nitrogen oxides. Up to 400 ppm of ozone and 100 ppm of NO_2, respectively, were measured within the filament volume [10, 12], leading to the local formation of hygroscopic HNO_3 in ppm concentration. The latter was also detected as NO_3^- ions dissolved in laser-induced particles of various sizes [12], as well as in laser-induced snowflakes [82], evidencing the role of binary H_2O–HNO_3 nucleation [19, 91, 92], similar to the binary H_2SO_4–H_2O condensation [14, 29] (see section 2.1.2).

The very complex chemistry occurring in air plasmas [93, 94] and the lack of data on the initial concentrations of species such as N^*, N_2^*, N^+ and N_2^+ in the filaments do not allow one to isolate a single scheme for HNO_3 formation. However, one of the main pathways is likely to rely on the fast reaction of N^+ ions with O_2, which at 43% yields [95]

$$N^+ + O_2 \rightarrow NO^+ + O^\bullet. \qquad (14)$$

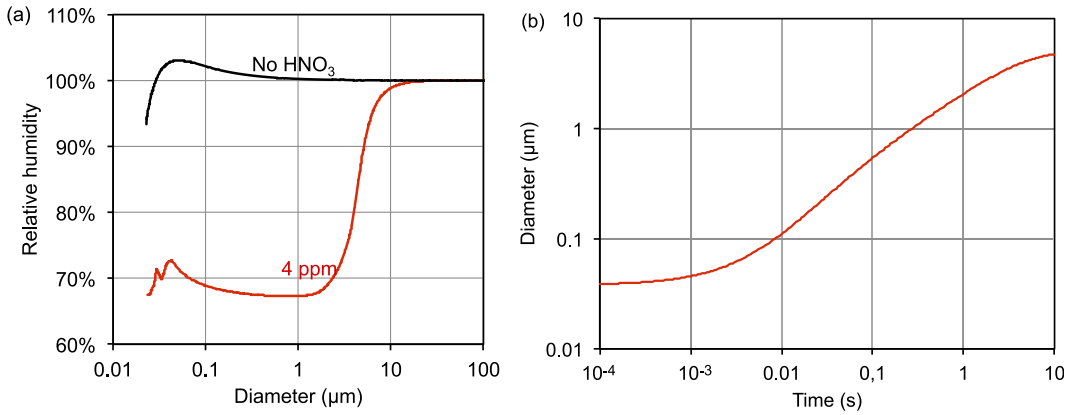

Figure 8. Laser-induced stabilization and growth of a cloud of 1000 particle cm^{-3}. (*a*) Köhler plot at 6 °C; (*b*) growth of ternary HNO_3–H_2O–NH_4NO_3 particles at 2 °C, 90% RH and 4 ppm HNO_3 (after [12]).

The oxygen radical $O^\bullet$ immediately reacts with O_2 to form ozone, which in turn oxidizes the NO^+ ion, after it captures a free electron:

$$O^\bullet + O_2 + M \rightarrow O_3 + M, \quad (15)$$

$$NO + O_3 \rightarrow NO_2 + O_2, \quad (16)$$

$$NO_2 + O_3 \rightarrow NO_3 + O_2. \quad (17)$$

The resulting high concentrations of NO_2 and NO_3 allow efficient formation of N_2O_5 [14], which immediately reacts with water:

$$NO_2 + NO_3 + M \rightleftarrows N_2O_5 + M, \quad (18)$$

$$N_2O_5 + H_2O(s) \rightarrow 2HNO_3. \quad (19)$$

The limiting reaction in this chain is reaction (9), with $k_{17} = 3 \times 10^{-17}$ cm^3 s^{-1} [14], which together with the extremely high NO_2 and ozone concentrations in the filaments can generate HNO_3 in the ppm range.

4.2. Semi-quantitative modelling of particle stability and growth

This HNO_3-mediated pathway is supported by numerical modelling. Figure 8(*a*) Displays the Köhler plot for ternary HNO_3–H_2O–NH_4NO_3 particles. The Köhler curve displays the equilibrium water saturation ratio S_{eq} over spherical particles as a function of their size, as defined by equation (9). Particles below the curve will tend to evaporate, while particles above the curve will grow until they reach one of its ascending branches. The equilibrium between evaporation and growth is stable on ascending branches of the Köhler curve, and unstable at maxima and on descending branches. S_{eq} reduces down to 70% in the presence of 4 ppm of HNO_3, a typical concentration in the laser filaments. Particles above a few tens of nm can grow until they reach the ascending branch of the Köhler curve at a size of several μm. This effect persists up to 30 °C, although its efficiency progressively decreases when the temperature increases. Conversely, the HNO_3 concentration in the air has only a moderate influence on the cut-off size of the Köhler plot. Its dilution therefore influences the droplet stabilization only marginally. This makes the model robust with regard to this parameter, which is hardly accessible experimentally.

In addition to stabilizing particles at RH well below 100%, the laser-generated HNO_3 drastically speeds up their growth. This acceleration is reproduced well by a kinetic model [96] adapted to multi-ppm HNO_3 concentrations. Laser-induced particles typically reach a micrometre-sized diameter within ~1 s or less (figure 8(*b*)), much faster than allowed by natural processes [14]. HNO_3 first accumulates in the particles during the first 10 ms of their growth. It is then diluted by efficient water uptake from the gas phase. The droplet growth is ultimately limited by both the amount of HNO_3 produced by the laser filaments and by the available humidity. Substantial water vapour depletion occurs as soon as the droplets exceed a few μm in diameter, so that the formation of micrometric particles is in correlation with the water VMR (see figure 7).

In spite of their successes, these models of laser-induced condensation deserve further enhancements to reach completeness. From the physical point of view, polydisperse size distributions should be taken into account. A full dynamic model should also be free of the steady-state approximation and include charge-accelerated coagulation of particles of sub-100 nm size, which could explain the fast appearance of micrometre-sized particles.

From the chemical point of view, a comprehensive model should include the influence of H_2SO_4 produced by the laser by oxidizing the background atmospheric SO_2 [14, 18, 19, 29], the contribution of hygroscopic H_2O_2 and mid-IR atmospheric photochemistry [97], including the excitation of organic peroxyl radicals (RO_2) [98] or water-cluster-mediated chemistry [99]. These radicals, originating from the VOCs present in the atmosphere, subsequently generate hydroxyl (OH) or hydroperoxyl (HO_2) radicals that are known to contribute to ozone formation. HO_2 radicals, which were also measured under UV illumination in concentrations exceeding 200 ppb, are produced by the reaction of ozone with OH radicals [90] and subsequently form hydrogen peroxide H_2O_2, a stable and highly hygroscopic molecule efficient in capturing water molecules. Finally, the influence of charge-transfer complexes of $H_2O^+O_2^-$ should be investigated [100].

Furthermore, a full understanding of laser-induced condensation requires considering not only particle growth, but

also their nucleation from the gas phase. Both homogeneous nucleation, with possible heteromolecular contributions of H_2SO_4 and HNO_3, and heterogeneous nucleation on mineral or organic condensation nuclei have to be considered. The latter may be activated and made hygroscopic [101–103] by the laser-generated ozone or HNO_3 [10, 14], allowing heterogeneous condensation.

5. Discussion: applicability of laser-induced condensation to cloud seeding

The demonstration of laser-induced condensation raises the question of its applicability and relevance to cloud seeding. By producing particles doped with hygroscopic HNO_3 with sub-micrometre to multi-micrometre size comparable to that produced by pyrotechnic flares [104], the laser filaments may be expected to offer artificial CCN and hence to promote the coalescence process in convective clouds. Hygroscopic seeding appears as the most robust cloud seeding technique, with both the most convincing statistical evidence of rainfall increase [104] and support by microphysical modelling [105, 106] defining the conditions under which efficient seeding can be expected.

Hygroscopic cloud seeding investigations in the atmosphere have shown that major limitations of this technique are the dispersion of the seeding particles, and the risk to provide an excess of these particles, locally reducing precipitation. This is due to the formation of too many small droplets competing for the available water vapour, so that their growth is limited and they remain too small to undergo droplet collision and coalescence [107].

In that regard, lasers might offer the opportunity to generate artificial CCN along their beam, with a relatively low local density that further reduces quickly due to dilution from the tiny volume of the laser filaments (typically in the cm^3 range for a TW laser beam) into the open atmosphere. This density can, moreover, be finely tuned by adjusting the laser power and the duration of its operation. On the other hand, laser beams can be swept across the forming clouds, in which filaments are known to propagate with little perturbation besides the losses due to the scattering of the photon bath [49]. This could allow precisely defining the regions of the cloud where the artificial CCNs would be released. Alternatively, purposely injecting an excess of CCNs could provide a means to temporally reduce precipitation.

Furthermore, the more-than-linear scaling up of the particle generation with the input laser energy [84] may raise the hope for the possibility of effectively seeding large cloud volumes. Considering the evolution of laser technology, such favourable dependence on laser energy could be efficiently exploited in the future [108]. The commercially available laser power has increased by two orders of magnitude over the last decade, reaching 250 TW nowadays, as compared with a few TW only ten years ago. Peak powers up to the exawatt are even expected in the foreseeable future at the Extreme Light Infrastructure [109].

However, quantitatively assessing both the feasibility of laser-based hygroscopic cloud seeding and its large-scale deployment needs further experimental data as well as theoretical work and modelling. In addition to this ultimate dream of seeding clouds, laser-induced condensation may also prove very useful in atmospheric precipitation research by offering new means of mapping the thermodynamic state of the atmosphere in three dimensions, and especially the possibility of nucleation and/or condensation within it. Such sensing could be performed in a pump-probe Lidar configuration, as described above (see figure 4(*c*)), in which a classical Lidar, with its beam superposed with that of ultrashort pulses generating laser filaments, sounds in real time the particles generated by the filaments [11]: their size and number density strongly depend on local, or even micro-local conditions. Such information could, for example, help in improving high-resolution weather forecast, or better understanding the process of cloud formation and precipitation.

6. Conclusion and outlook

The last two years have seen the emergence of laser-induced water condensation in the atmosphere as a new potential field of application for ultrashort laser pulses, which might have a strong impact on cloud seeding. The observation of the phenomenon under various conditions by several groups is now well established, and some basic processes at play are identified. However, understanding the full complexity of the different pathways contributing to this mechanism constitutes the most challenging question ahead in this field. Both aerosol microphysics and plasma photochemistry have to provide a deeper view and understanding of laser-generated particles from their nucleation to their ultimate evolution.

The second challenge ahead regards the potential application of these results to the atmospheric seeding of clouds. Assessing its feasibility on a sufficiently large scale requires further knowledge on the efficiency of laser-induced condensation under various atmospheric conditions, which would enable realistic modelling of the observed particle nucleation and growth, and allow the determination of cloud types, regions and conditions in which precipitation enhancement may be expected. Finally, the ability of the lasers to seed macroscopic cloud volumes has to be confirmed, so as to define realistic strategies for beam emission and sweeping. These strategies will then have to be tested in real scale during atmospheric campaigns.

Acknowledgments

Most of our results discussed in this review have involved members of the Teramobile team, especially at the Free University of Berlin, University of Lyon and University of Geneva. We would like to thank them for our excellent collaboration and common work. This work was supported by the Swiss NSF (Grant No 20021-125315).

References

[1] Zikeev N T and Doumani G A 1967 *Weather Modification in the Soviet Union, 1946–1966; A Selected Annotated Bibliography* (Washington, DC: Library of Congress, Science Technology Division)

[2] Langmuir I 1947 Growth of particles in smokes and clouds and the production of snow from supercooled clouds *Science* **106** 505

[3] Schaefer V J 1950 Localized effects induced by seeding supercooled clouds with dry ice and silver iodide *Science* **112** 447–56

[4] Schaefer V J 1946 The production of ice crystals in a cloud of supercooled water droplets *Science* **104** 457–9

[5] Simpson J, Brier G W and Simpson R H 1967 Stormfury cumulus seeding experiment 1965: Statistical analysis and main results *J. Atmos. Sci.* **24** 508–21

[6] Saleeby S M, Cotton W R and Fuller J D 2011 The cumulative impact of cloud droplet nucleating aerosols on orographic snowfall in Colorado *J. Appl. Meteor. Climatol.* **50** 604–25

[7] Bruintjes R T 1999 A review of cloud seeding experiments to enhance precipitation and some new prospects *Bull. Am. Meteor. Soc.* **80** 805–20

[8] Qiu J and Cressey D 2008 Taming the sky *Nature* **453** 970–4

[9] US National Research Council 2003 *Critical Issues in Weather Modification Research* (Washington, DC: National Academies)

[10] Petit Y, Henin S, Kasparian J and Wolf J-P 2010 Production of ozone and nitrogen oxides by laser filamentation *Appl. Phys. Lett.* **97** 021108

[11] Rohwetter P *et al* 2010 Laser-induced water condensation in air *Nature Photon.* **4** 451–6

[12] Henin S *et al* 2011 Field measurements suggest mechanism of laser-assisted water condensation *Nature Commun.* **2** 456

[13] Pruppacher H R and Klett J D 1997 *Microphysics of Clouds and Precipitation* (Dordrecht: Kluwer)

[14] Seinfeld J H and Pandis S N 2006 *Atmospheric Chemistry and Physics—From Air Pollution to Climate Change* 2nd edn (Hoboken, NJ: Wiley)

[15] Denbigh K 1981 *The Principles of Chemical Equilibrium* 4th edn (Cambridge: Cambridge University Press)

[16] Yu F 2005 Modified Kelvin–Thomson equation considering ion-dipole interaction: Comparison with observed ion-clustering enthalpies and entropies *J. Chem. Phys.* **122** 084503–8

[17] Reiss H 1950 The kinetics of phase transitions in binary systems *J. Chem. Phys* **18** 840

[18] Yu F and Turco F P 2001 From molecular clusters to nanoparticles: Role of ambient ionization in tropospheric aerosol formation *J. Geophys. Res.* **106** 4797–814

[19] Yu F 2006 From molecular clusters to nanoparticles: second-generation ion-mediated nucleation model *Atmos. Chem. Phys.* **6** 5193–211

[20] Jaenicke R 1993 Tropospheric aersosols *Aerosol–Cloud–Climate Interactions* ed P V Hobbs (Burlington, MA: Academic) pp 1–31

[21] Metzger A *et al* 2010 Evidence for the role of organics in aerosol particle formation under atmospheric conditions *Proc. Natl Acad. Sci.* **107** 6646–51

[22] Spracklen D V *et al* 2008 Contribution of particle formation to global cloud condensation nuclei concentrations *Geophys. Res. Lett.* **35** L06808

[23] Hobbs P V 1993 Aerosol–cloud interactions *Aerosol–Cloud–Climate Interactions* ed Hobbs (Burlington, MA: Academic) pp 33–73

[24] Wilson C T R 1911 On a method of making visible the paths of ionising particles through a Gas *Proc. R. Soc. Lond.* A **85** 285–8

[25] Thomson J J 1906 *Conduction of Electricity through Gases* (London: Cambridge University Press)

[26] Tohmfor G and Volmer M 1938 Die Keimbildung unter dem Einfluß elektrischer Ladungen *Ann. Phys.* **425** 109–31

[27] Pérez A and Rubio A 2011 A molecular dynamics study of water nucleation using the TIP4P/2005 model *J. Chem. Phys.* **135** 244505

[28] Hirsikko A *et al* 2011 Atmospheric ions and nucleation: a review of observations *Atmos. Chem. Phys.* **11** 767–98

[29] Duplissy J *et al* 2010 Results from the CERN pilot CLOUD experiment *Atmos. Chem. Phys.* **10** 1635–47

[30] Braun A, Korn G, Liu X, Du D, Squier J and Mourou G 1995 Self-channeling of high-peak-power femtosecond laser pulses in air *Opt. Lett.* **20** 73–5

[31] Couairon A and Mysyrowicz A 2007 Femtosecond filamentation in transparent media *Phys. Rep.* **441** 47–189

[32] Bergé L, Skupin S, Nuter R, Kasparian J and Wolf J-P 2007 Ultrashort filaments of light in weakly-ionized, optically-transparent media *Rep. Prog. Phys.* **70** 1633–713

[33] Chin S L *et al* 2005 The propagation of powerful femtosecond laser pulses in optical media: physics, applications, and new challenges *Can. J. Phys.* **83** 863–905

[34] La Fontaine B, Vidal F, Jiang Z, Chien C Y, Comtois D, Desparois A, Johnson T W, Kieffer J-C and Pépin H 1999 Filamentation of ultrashort pulse laser beams resulting from their propagation over long distances in air *Phys. Plasmas* **6** 1615–21

[35] Becker A, Aközbek N, Vijayalakshmi K, Oral E, Bowden C M and Chin S L 2001 *Appl. Phys.* B **73** 287

[36] Daigle J-F, Jaron-Becker A, Hosseini S, Wang T-J, Kamali Y, Roy G, Becker A and Chin S L 2010 Intensity clamping measurement of laser filaments in air at 400 and 800 nm *Phys. Rev.* A **82** 023405

[37] Kasparian J, Sauerbrey R and Chin S L 2000 *Appl. Phys.* B **71** 877

[38] Béjot P, Kasparian J, Henin S, Loriot V, Vieillard T, Hertz E, Faucher O, Lavorel B and Wolf J-P 2010 Higher-order Kerr terms allow ionization-free filamentation in gases *Phys. Rev. Lett.* **104** 103903

[39] Béjot P, Hertz E, Lavorel B, Kasparian J, Wolf J-P and Faucher O 2011 Transition from plasma- to Kerr-driven laser filamentation *Phys. Rev. Lett.* **106** 243902

[40] Shen Y R 1984 *The Principles of Nonlinear Optics* (New York: Wiley-Interscience) pp 303–24

[41] Méjean G, Kasparian J, Yu J, Salmon E, Frey S, Wolf J-P, Skupin S, Vinçotte A, Nuter R, Champeaux S and Bergé L 2005 Multifilamentation transmission through fog *Phys. Rev.* E **72** 026611

[42] Henin S *et al* 2010 Saturation of the filament density of ultrashort intense laser pulses in air *Appl. Phys.* B **100** 77

[43] Petit Y *et al* 2011 1-J white-light continuum from 100-TW laser pulses *Phys. Rev.* A **83** 013805

[44] Rodriguez M *et al* 2004 Kilometer-range non-linear propagation of femtosecond laser pulses *Phys. Rev.* E **69** 036607

[45] Méchain G, Couairon A, André Y-B, D'Amico C, Franco M, Prade B, Tzortzakis S, Mysyrowicz A and Sauerbrey R 2004 Long-range self-channeling of infrared laser pulses in air: a new propagation regime without ionization *Appl. Phys.* B **79** 379

[46] Wille H, Rodriguez M, Kasparian J, Mondelain D, Yu J, Mysyrowicz A, Sauerbrey R, Wolf J-P and Wöste L 2002 Teramobile: a mobile femtosecond-terawatt laser and detection system *Eur. Phys. J.—Appl. Phys.* **20** 183–90

[47] Strickland D and Mourou G 1985 Compression of amplified chirped optical pulses *Opt. Commun.* **56** 219

[48] Liu W, Théberge F, Arévalo E, Gravel J-F, Becker A and Chin S L 2005 Experiment and simulations on the energy reservoir effect in femtosecond light filaments *Opt. Lett.* **30** 2602–4

[49] Courvoisier F, Boutou V, Kasparian J, Salmon E, Méjean G, Yu J and Wolf J-P 2003 Light filaments transmitted through clouds *Appl. Phys. Lett.* **83** 213–5

[50] Kolesik M and Moloney J V 2004 Self-healing femtosecond light filaments *Opt. Lett.* **29** 590–2

[51] Skupin S, Bergé L, Peschel U and Luderer F 2004 Interaction of femtosecond light filaments with obscurants in aerosols *Phys. Rev. Lett.* **93** 023901

[52] Méchain G *et al* 2005 Propagation of fs-TW laser filaments in adverse atmospheric conditions *Appl. Phys.* B **80** 785–9

[53] Ackermann R, Méjean G, Kasparian J, Yu J, Salmon E and Wolf J-P 2006 Laser filaments generated and transmitted in highly turbulent air *Opt. Lett.* **31** 86–8

[54] Salamé R, Lascoux N, Salmon E, Kasparian J and Wolf J P 2007 Propagation of laser filaments through an extended turbulent region *Appl. Phys. Lett.* **91** 171106

[55] Kasparian J *et al* 2003 White-light filaments for atmospheric analysis *Science* **301** 61–4

[56] Kasparian J and Wolf J-P 2008 Physics and applications of atmospheric nonlinear optics and filamentation *Opt. Express* **16** 466–93

[57] Kamali Y *et al* 2009 Remote sensing of trace methane using mobile femtosecond laser system of *T&T* Lab *Opt. Commun.* **282** 2062–5

[58] Alfano R R 2006 *The Supercontinuum Laser Source: Fundamentals with Updated References* (New York: Springer)

[59] Maioli P, Salamé R, Lascoux N, Salmon E, Béjot P, Kasparian J and Wolf J-P 2009 Ultraviolet-visible conical emission by multiple laser filaments *Opt. Express* **17** 4726–31

[60] Théberge F, Châteauneuf M, Ross V, Mathieu P and Dubois J 2008 Ultrabroadband conical emission generated from the ultraviolet up to the far-infrared during the optical filamentation in air *Opt. Lett.* **33** 2515–7

[61] Measures R M 1984 *Laser Remote Sensing—Fundamentals and applications* (New York: Wiley-Interscience)

[62] Méjean G *et al* 2003 Towards a supercontinuum-based infrared Lidar *Appl. Phys.* B **77** 357–9

[63] Galvez M C, Fujita M, Inoue N, Moriki R, Izawa Y and Yamanaka C 2002 Three-wavelength backscatter measurement of clouds and aerosols using a white light lidar system *Japan. J. Appl. Phys.* **41** L284–6

[64] Bourayou R *et al* 2005 White-light filaments for multiparameter analysis of cloud microphysics *J. Opt. Soc. Am.* B **22** 369

[65] Méjean G, Kasparian J, Yu J, Frey S, Salmon E and Wolf J-P 2004 Remote detection and identification of biological aerosols using a femtosecond terawatt lidar system *Appl. Phys.* B **78** 535–7

[66] Hill S C, Boutou V, Yu J, Ramstein S, Wolf J-P, Pan Y-L, Holler S and Chang R K 2000 Enhanced backward-directed multiphoton-excited fluorescence from dielectric microspheres *Phys. Rev. Lett.* **85** 54–7

[67] Luo Q, Xu H L, Hosseini S A, Daigle J F, Theberge F, Sharifi M and Chin S L 2006 Remote sensing of pollutants using femtosecond laser pulse fluorescence spectroscopy *Appl. Phys.* B **82** 105–9

[68] Gravel J-F, Luo Q, Boudreau D, Tang X P and Chin S L 2004 *Anal. Chem.* **76** 4799

[69] Stelmaszczyk K, Rohwetter P, Méjean G, Yu J, Salmon E, Kasparian J, Ackermann R, Wolf J-P and Wöste L 2004 Long-distance remote LIBS using filamentation in air *Appl. Phys Lett.* **85** 3977

[70] Tzortzakis S, Anglos D and Gray D 2006 Ultraviolet laser filaments for remote laser-induced breakdown spectroscopy (LIBS) analysis: applications in cultural heritage monitoring *Opt. Lett.* **31** 1139–41

[71] Chin S L *et al* 2009 Filamentation 'remote' sensing of chemical and biological agents/pollutants using only one femtosecond laser source *Appl. Phys.* B **95** 1–12

[72] Uchida S, Shimada Y, Yasuda H, Motokoshi S, Yamanaka C, Yamanaka T, Kawasaki Z and Tsubakimoto K 1999 Laser-triggered lightning in field experiments *J. Opt. Technol.* **66** 199

[73] Apollonov V, Kazakov K, Pletnyev N and Sorochenko V *AHPLA'99* Paper 3886–34

[74] Pépin H *et al* 2001 Triggering and guiding high-voltage large-scale leader discharges with sub-joule ultrashort laser pulses *Phys. Plasmas* **8** 2532–9

[75] Rodriguez M *et al* 2002 Megavolt discharges triggered and guided with laser filaments *Opt. Lett.* **27** 772–4

[76] Rambo P, Schwarz J and Diels J-C 2001 High-voltage electrical discharges induced by an ultrashort-pulse UV laser system *J. Opt. A: Pure Appl. Opt.* **3** 146–58

[77] Méjean G *et al* 2006 Improved laser triggering and guiding of megavolt discharges with dual fs-ns pulses *Appl. Phys. Lett.* **88** 021101

[78] Liu X-L *et al* 2012 Long lifetime air plasma channel generated by femtosecond laser pulse sequence *Opt. Express* **20** 5968–73

[79] Kasparian J *et al* 2008 Electric events synchronized with laser filaments in thunderclouds *Opt. Express* **16** 5757–63

[80] Kasparian J *et al* 2008 Progress towards lightning control using lasers *J. Eur. Opt. Soc.: Rapid Publ.* **3** 08035

[81] Sugiyama K, Fujii T, Miki M, Yamaguchi M, Zhidkov A, Hotta E and Nemoto K 2009 Laser-filament-induced corona discharges and remote measurements of electric fields *Opt. Lett.* **34** 2964–6

[82] Ju J, Liu J, Wang C, Sun H, Wang W, Ge X, Li C, Chin S L, Li R and Xu Z 2012 Laser-filamentation-induced condensation and snowfall in a cloud chamber *Opt. Lett.* **37** 1214

[83] Yoshihara K 2005 Laser-induced mist and particle formation from ambient air: a possible new cloud seeding method *Chem. Lett.* **34** 1370

[84] Petrarca M *et al* 2011 Multijoule scaling of laser-induced condensation in air *Appl. Phys. Lett.* **99** 141103

[85] Méjean G *et al* 2005 *Phys. Rev.* E **72** 026611

[86] Yoshino K, Parkinson W H, Ito K and Matsui T 2005 *J. Mol. Spectosc.* **229** 238

[87] Petit Y *et al* 2011 Influence of pulse duration, energy, and focusing on laser-assisted water condensation *Appl. Phys. Lett.* **98** 041105

[88] Richards P G, Torr D G and Torr M R 1981 *J. Geophys. Res.* **86** 1495

[89] Zipf E C, Espy P J and Boyle C F 1980 *J. Geophys. Res.* **85** 687

[90] Yoshihara K, Takatori Y, Miyazaki K and Kajkii Y 2007 Ultraviolet light-induced water-droplet formation from wet ambient air *Proc. Japan Acad.* B **83** 320–5

[91] Kerminen V-M, Wexler A S and Potukuchi S 1997 Growth of freshly nucleated particles in the troposphere: roles of NH_3, H_2SO_4, HNO_3, and HCl *J. Geophys. Res.* **102** D3 3715–24

[92] Koop T, Luo B, Biermann U M, Crutzen P J and Peter T 1997 *J. Phys. Chem.* A **101** 1117–33

[93] Kossyi I A, Kostinsky A Y, Matveyev A A and Silakov V P 1992 Kinetic scheme of the non-equilibrium discharge in nitrogen–oxygen mixtures *Plasma Sources Sci. Technol.* **1** 207–21

[94] Xu H L, Azarm A, Bernhardt J, Kamali Y and Chin S L 2009 *Chem. Phys.* **360** 171

[95] Dotan I, Hierl P M, Morris R A and Viggiano A A 1997 *Int. J. Mass Spectrom. Ion Process.* **167/168** 223–30

[96] Kulmala M, Laaksonen A, Korhonen P, Vesala T, Ahonen T and Barrett J C 1993 The effect of atmospheric nitric acid vapor on cloud condensation nucleus activation *J. Geophys. Res.* **98** 22949–58

[97] Donaldson D J, George C and Vaida V 2010 *Environ. Sci. Technol.* **44** 5321
[98] Frost G J, Ellison G B and Vaida V 1999 *J. Phys. Chem.* A **103** 10169
[99] Vaida V 2011 *J. Chem. Phys.* **135** 020901
[100] Byers Brown W 1995 *Chem. Phys. Lett.* **235** 94
[101] Wyslouzil B E, Carleton K L, Sonnenfroh D M, Rawlins W T and Arnold S 1994 Observation of hydration of single, modified carbon aerosols *Geophys. Res. Lett.* **21** 2107–10
[102] Vlasenko A, Sjogren S, Weingartner E, Stemmler K, Gäggeler H W and Ammann M 2006 Effect of humidity on nitric acid uptake to mineral dust aerosol particles *Atmos. Chem. Phys.* **6** 2147–60
[103] Schwier A, Sareen N, Lathem T, Nenes A and McNeill V F 2011 Ozone oxidation of oleic acid surface films decreases aerosol cloud condensation nuclei activity *J. Geophys. Res.* **116** D16202
[104] Mather G K, Terblanche D E, Steffens F E and Fletcher L 1997 Results of the South African cloud-seeding experiments using hygroscopic flares *J. Appl. Meteorol.* **36** 1433–47
[105] Reisin T, Tzivion S and Levin Z 1996 Seeding convective clouds with ice nuclei or hygroscopic particles: a numerical study using a model with detailed microphysics *J. Appl. Meteorol.* **35** 1416–34
[106] Cooper W A, Bruintjes R T and Mather G K 1997 Some calculations pertaining to hygroscopic seeding with flares *J. Appl. Meteorol.* **36** 1449–69
[107] Levin Z and Cotton W R 2009 *Aerosol Pollution Impact on Precipitation: A Scientific Review* (Heidelberg: Springer)
[108] Hecht J 2011 Photonics frontiers: The Extreme Light Infrastructure: The ELI aims to break down the vacuum *Laser Focus World* 01/2011
[109] Chambaret J-P *et al* 2010 Extreme Light Infrastructure: architecture and major challenges *Proc. SPIE* **7721** 77211D